View metadata, citation and similar papers at core.ac.uk

brought to you by CORE

provided by Elsevier - Publisher Connector

Remote Sensing of Environment 136 (2013) 37–46

Contents lists available at SciVerse ScienceDirect

Remote Sensing of Environment

journal homepage: www.elsevier.com/locate/rse

Quantifying the heat flux and outflow rate of hot springs using airborne thermal imagery: Case study from Pilgrim Hot Springs, Alaska

Christian Haselwimmer [a,*], Anupma Prakash [a], Gwen Holdmann [b]

[a] Geophysical Institute, University of Alaska Fairbanks, Fairbanks, AK, USA
[b] Alaska Center for Energy and Power, University of Alaska Fairbanks, Fairbanks, AK, USA

ARTICLE INFO

Article history:
Received 7 February 2013
Received in revised form 15 April 2013
Accepted 18 April 2013
Available online 20 May 2013

Keywords:
Thermal infrared
FLIR
Hot springs
Heat flux
Outflow rate
Geothermal
Heat-loss
Pilgrim Hot Springs
Alaska
Resource assessment
Monitoring

ABSTRACT

In undertaking heat loss studies of geothermal systems, it is important to consider the heat flux associated with the outflow of thermal waters at hot springs, which may account for over 50% of the total natural surface heat loss. Conventional in-situ methods for quantifying hot spring heat flux may not always be feasible if there are low rates of flow or thermal waters are not confined to well-defined drainage channels. This paper describes the use of high spatial resolution airborne thermal infrared (TIR) imagery for quantifying the heat flux and corresponding outflow rate of hot springs using a case study of the Pilgrim Hot Springs geothermal system in western Alaska. The approach is based upon the use of a simplified, steady-state, heat budget model that describes the heat gains and losses from areas of thermal water to calculate the hot spring heat flux required to maintain the temperature of these waters above ambient conditions. Inputs to the model include calibrated surface temperature maps for areas of thermal water derived from processing of airborne TIR imagery acquired using a broadband forward looking infrared (FLIR) camera as well various atmospheric variables relevant to the thermodynamics of water bodies. The model is applied on a per-pixel basis to provide maps of the hot spring heat flux for the thermal waters. The total hot spring heat flux, representing the sum of the per-pixel heat fluxes, is used to calculate a corresponding hot spring outflow rate assuming a fixed hot spring temperature. This approach has been applied to TIR imagery acquired during two surveys over Pilgrim Hot Springs in Fall 2010 and Spring 2011. Although the heat budget model is particularly sensitive to wind speed, the results provide conservative estimates of the hot spring heat flux and outflow rates (at 81.3 °C) of ~4.7–6.7 MW thermal energy, and ~976–1400 l/min, respectively. These results are 2–3 times higher than field-based estimates of the hot spring heat flux derived using direct measurements of the flow rate in streams draining part of the thermal catchment at the site. This result is consistent with the synoptic capabilities of the airborne TIR data that map all areas of thermal water. This approach has significant potential as a rapid and repeatable method for quantitative investigations of spring-dominated geothermal systems in support of resource assessment, and long-term monitoring.

© 2013 The Authors. Published by Elsevier Inc. Open access under CC BY license.

1. Introduction

Geothermal systems are associated with areas of anomalously high crustal heat flow that may be related to the presence of young igneous bodies or occur where hot basement rocks are located at relatively shallow depths in regions of crustal extension. In most geothermal systems that have sufficient heat, water, and permeability, hydrothermal circulation provides the mechanism by which thermal energy is transferred to the Earth's surface. As hot fluids rise, heat is lost by conduction to the surrounding bedrock that leads to the development of thermal aureoles, which may be manifested as ground surface temperature anomalies. If hot fluids have not cooled completely by the time they reach the Earth's surface then heat loss via convection produces characteristic surface hydrothermal features such as hot springs, geysers, and steaming ground. Total surface heat loss is the sum of thermal energy lost by conductive and convective processes that is an important state variable describing the size and activity of a geothermal system. This can be used to predict the power potential of undeveloped geothermal systems using empirical relationships between surface heat loss and electrical production capacity established from developed resources (Wisian et al., 2001). The monitoring of surface heat loss can also contribute to the management of geothermal power plants by providing boundary conditions for reservoir models and potential surface indicators of unsustainable fluid extraction (Bromley et al., 2011). In the case of hydrothermal activity associated with volcanic systems, such as Yellowstone National Park, the monitoring of surface heat loss and thermal features provides one approach to monitoring the long-term

* Corresponding author. Tel.: +1 907 474 7676.
E-mail address: chha@gi.alaska.edu (C. Haselwimmer).

0034-4257 © 2013 The Authors. Published by Elsevier Inc. Open access under CC BY license.
http://dx.doi.org/10.1016/j.rse.2013.04.008

activity of the deeper volcanic source (Vaughan et al., 2012), as well as potential anthropogenic disturbances related to geothermal fluid production (Heasler et al., 2009).

Although conductive heat loss predominates (Wisian et al., 2001), the outflow of thermal waters can account for over 50% of the total natural surface heat loss (Richards & Blackwell, 2002). Quantifying this heat flux is therefore important for estimation of the total surface heat loss from geothermal systems. Determining the heat flux associated with hot springs is conventionally undertaken using in-situ measurement of the volumetric flow rate and temperature of thermal waters within channels draining geothermal areas (Heasler et al., 2009) or using geochemical approaches such as the chloride-inventory method (Ellis & Wilson, 1955). While these methods are often reliable (see for example: Ingebritsen et al., 2001) they suffer from limitations; direct measurement of hot spring outflow rates requires that the thermal waters be confined in well-defined drainage channels (i.e. thermal streams; Fig. 1) enabling velocity–area measurements to be recorded using current meters or with emplacing weirs or flumes. In the case of hot springs with low outflow rates, numerous distributed springs/seeps or poorly confined drainage channels, these approaches may be difficult to undertake. The chloride-inventory method utilizes the often elevated chloride load of geothermal fluids to measure the total outflow based upon downstream increases in the solute within nearby streams (Ellis & Wilson, 1955). This involves measuring the chloride concentration upstream and downstream of the point where thermal waters are discharged into a non-geothermal stream or river. The method therefore requires that thermal waters be confined in well-defined channels that join nearby non-geothermal drainages. Given these constraints, the chloride-inventory method may be inappropriate for hot springs where there are low outflow rates, poorly defined thermal streams or where there is an absence of obvious flow into secondary non-geothermal channels.

This paper describes an alternative method for quantifying the heat flux and outflow rate of hot springs using airborne thermal infrared (TIR) imagery acquired with a broadband forward looking infrared (FLIR) camera. The method employs a steady-state thermal budget model that describes the heat inputs and outputs from a body of water. Using the measured surface temperature values for thermal waters derived from the TIR imagery as input and accounting for heat gains and losses due to various mechanisms, the heat flux required to maintain the temperature of thermal waters above ambient conditions is calculated. This approach has been adapted and simplified from previous work on estimating the geothermal heat flux from volcanic crater lakes (Hernández et al., 2007; Oppenheimer, 1996) and mud volcanoes (Patrick et al., 2004) using satellite TIR and ground-based FLIR imagery. In this paper, we demonstrate the application of these techniques using airborne FLIR imagery to an undeveloped spring-dominated geothermal system with the specific aim of providing quantitative estimates of hot spring heat flux and outflow rate.

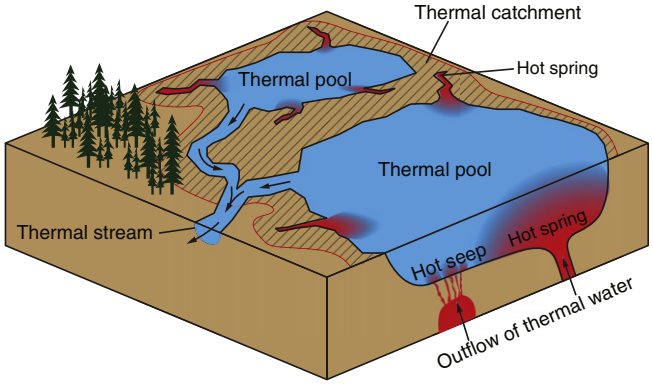

Fig. 1. Summary diagram of surface features associated with thermal water outflow at hot springs.

The study site for this research is Pilgrim Hot Springs, Alaska (164.924 W, 65.092 N) that is a low-to-moderate temperature geothermal system, which is being investigated as a potential power source for communities on the Seward Peninsula including the City of Nome (Fig. 2). The work described in this paper constitutes part of the exploration and resource assessment phase of this project that has included the use of satellite and airborne remote sensing for mapping surface geothermal phenomena and quantifying associated system heat losses. In this paper, we describe the use of multi-temporal airborne FLIR imagery acquired over Pilgrim Hot Springs to estimate the heat flux and outflow rate of the hot springs using the aforementioned thermal budget modeling approach. Pilgrim Hot Springs represents a good case study site to test these methods as the geothermal area encompasses numerous distributed hot springs and seeps with low rates of outflow whose total heat flux is difficult to measure directly using field-based techniques. As part of this work, the hot spring heat flux and outflow rate estimates derived from FLIR data were compared with the available in-situ measurements and a sensitivity analysis was performed to assess the impact of varying heat budget model parameters.

2. Background

2.1. Terminology

To provide consistency in the nomenclature the following terms are defined (Fig. 1): *thermal waters* are fluids that have been heated by a geothermal system and are thermally anomalous with respect to non-geothermal surface waters at ambient temperature. A *hot spring* is a well-defined outflow source of thermal waters at the Earth's surface. A *hot seep* is a type of hot spring where the outflow is less well defined and more diffuse in nature. A *thermal pool* is a body of standing thermal water that is fed by a number of hot springs or seeps. A *thermal catchment* represents the area containing hot springs, seeps, and thermal pools that contribute hot waters to a *thermal stream*, which is a drainage feature that carries thermal waters away from a geothermal area. The *hot spring heat flux* is the amount of thermal energy associated with the outflow of thermal waters at hot springs or seeps that in this paper is presented in units of megawatts (MW). In this research, the hot spring heat flux is the same as the heat flux associated with the surface thermal waters (pools and streams) as we assume the system is in steady-state and the hot springs/seeps are the only source of heat to the surface thermal waters. The *hot spring outflow rate* is the volume of thermal water discharged per unit of time.

2.2. TIR remote sensing of geothermal waters

The discrimination of temperature anomalies in TIR remote sensing data, particularly acquired by airborne instruments, has been well documented as a means of mapping surface geothermal features such as hot springs, fumaroles, and steaming or heated ground (see for example: Hodder, 1970; Mongillo, 1994; Seielstad & Queen, 2009). TIR imagery has also been used to estimate the heat loss associated with these geothermal features with satellite (Vaughan et al., 2012) and airborne data (Allis et al., 1999; Seielstad & Queen, 2009). Heat loss is commonly derived from TIR surface temperature data by calculating a radiative heat flux that represents radiation emitted from geothermal pixels corrected for that which would normally be emitted from a comparable surface at ambient temperatures. For thermal waters produced by hot springs, the radiative heat flux provides lower bounds on the hot spring heat flux sustaining the temperature of these waters as evaporation, sensible heat transfer, seepage, and overflow are also important heat loss mechanisms that govern the thermodynamics of water bodies (Oppenheimer, 1996). Using a simple steady-state thermal budget model describing heat gains and losses, the heat flux to a body of thermal water may be more accurately estimated. Following Obha et al. (1994) the

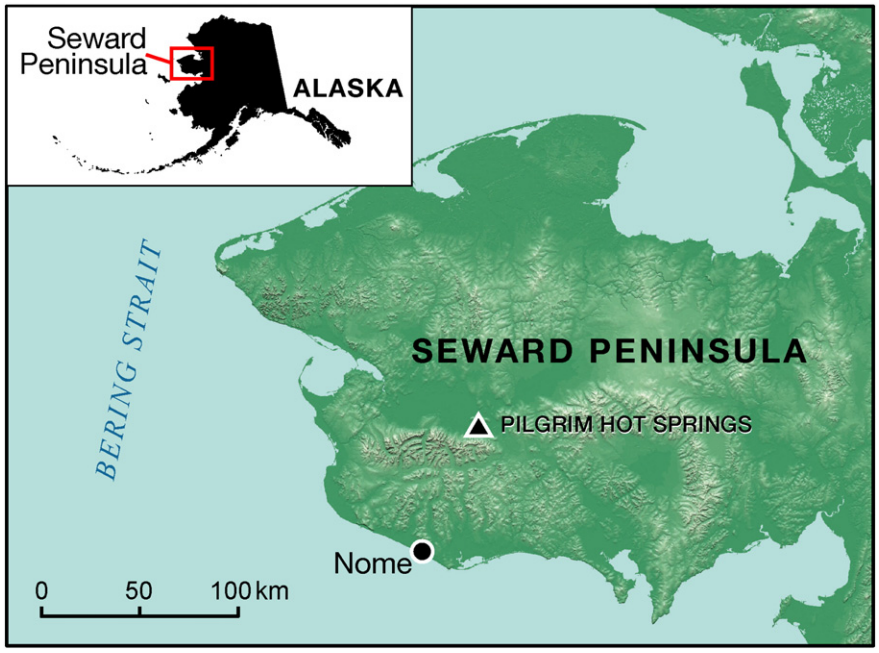

Fig. 2. Location of Pilgrim Hot Springs on the Seward Peninsula in western Alaska.

total thermal budget, Φ_{total}, (in W) for a body of water can be expressed as:

$$\Phi_{total} = \Phi_{ppt} + \Phi_{geo} + \Phi_{seep} + \Phi_{evap} + \Phi_{sens} + \Phi_{rad} + \Phi_{sun} + \Phi_{sky} \quad (1)$$

where Φ_{ppt}, Φ_{geo}, Φ_{seep}, Φ_{evap}, Φ_{sens}, Φ_{rad}, Φ_{sun}, and Φ_{sky} are heat fluxes associated with precipitation, geothermal fluids (i.e. the hot spring heat flux), seepage, evaporation, sensible heat, emitted radiation, incoming solar radiation, and incoming long-wave radiation from the atmosphere, respectively. TIR remote sensing provides information on the extent and skin temperature of water bodies that is a key determinant of the Φ_{evap}, Φ_{sens}, and Φ_{rad} terms (Oppenheimer, 1997b). Oppenheimer (1997a) applied a simplified version of this model, removing Φ_{ppt} and Φ_{seep} terms that were assumed to be negligible, to quantify the geothermal heat flux of six volcanic crater lakes in New Zealand, the Philippines, Indonesia, Costa Rica, and Nicaragua. Using Landsat Thematic Mapper (TM) thermal data converted to brightness temperature values, and estimates of wind speed, air temperature and humidity, the sensible, evaporative and radiative heat flux densities were calculated for crater-lake pixels. When coupled with estimates of incoming solar and longwave heat flux densities, the total geothermal heat flux for the crater lakes was determined by multiplying the flux densities by the pixel area and summing for the whole lake (Oppenheimer, 1997a). Patrick et al. (2004) applied the same approach using Landsat 7 Enhanced Thematic Mapper Plus (ETM+) TIR data to estimate the geothermal heat flux associated with active mud volcanoes in Southeastern Alaska. In this case, the areal extent of active mud discharge was smaller than the pixel size of the ETM+ TIR sensor (60 m) so the area and temperature of hot mud was determined by modeling the measured radiance as a linear mixture of hot mud and cool background components. The work described in this paper employed a similar thermal budget approach using high spatial resolution airborne TIR imagery acquired over Pilgrim Hot Springs, Alaska with the aim of determining the geothermal/hot spring heat flux sustaining areas of thermal water. Given the relatively low temperature and limited extent of thermal pools and streams at Pilgrim Hot Springs, high spatial resolution airborne data was critical for this work; at the spatial resolution of satellite TIR sensors these pools are not effectively resolved.

2.3. Pilgrim Hot Springs

Pilgrim Hot Springs is a low to moderate temperature geothermal system that is located on the Seward Peninsula in western Alaska around 75 km northeast of the City of Nome (Fig. 2). It is one of a number of spring-dominated geothermal systems that make up a broad E–W aligned swath of geothermal activity in central Alaska collectively referred to as the Central Alaskan Hot Springs Belt (Kolker, 2008). Pilgrim Hot Springs is located on the flood plain of the generally E–W meandering Pilgrim River that flows in the valley bottom north of the Kigluaik Mountains and south of Hen and Chickens and Mary's Mountain (Fig. 3). The geothermal area is outlined by an approximately two square mile zone of thawed permafrost characterized by dense brush and Cottonwood's that contrasts markedly with the surrounding stunted sub-Arctic vegetation growing on discontinuous permafrost (Wescott & Turner, 1981). In the geothermal area, numerous hot springs and seeps discharge saline thermal water at up to 81.3 °C (Fig. 4) that feed into thermal pools and streams draining the site. Extensive geological and geophysical research has been conducted at Pilgrim Hot Springs since the 1970s with the aim of evaluating its potential as a geothermal power resource (Turner & Forbes, 1980; Wescott & Turner, 1981). Most recently, this work has been undertaken as part of a jointly funded US Department of Energy (DOE) and Alaska Energy Authority (AEA) project that provides the context for the research described in this paper. Investigations of the geothermal system at Pilgrim Hot Springs indicate the presence of a shallow 90 °C geothermal aquifer located 15–35 m beneath the surface that is fed from deeper reservoirs of between 120–150 °C (Alaska Center for Energy & Power, 2012; Liss & Motyka, 1994). This shallow aquifer represents the source of thermal waters for the hot springs and seeps.

2.4. Geological context

Bounding normal faults to the north and south of the Pilgrim River valley indicate that it is located in a E–W aligned graben system (Turner & Forbes, 1980). The southern bounding fault represents the range front fault of the up to 1200 m elevation Kigluaik Mountains that has been active within the last 10,000 years. Exploration wells at the main hot springs site indicate a depth to basement of

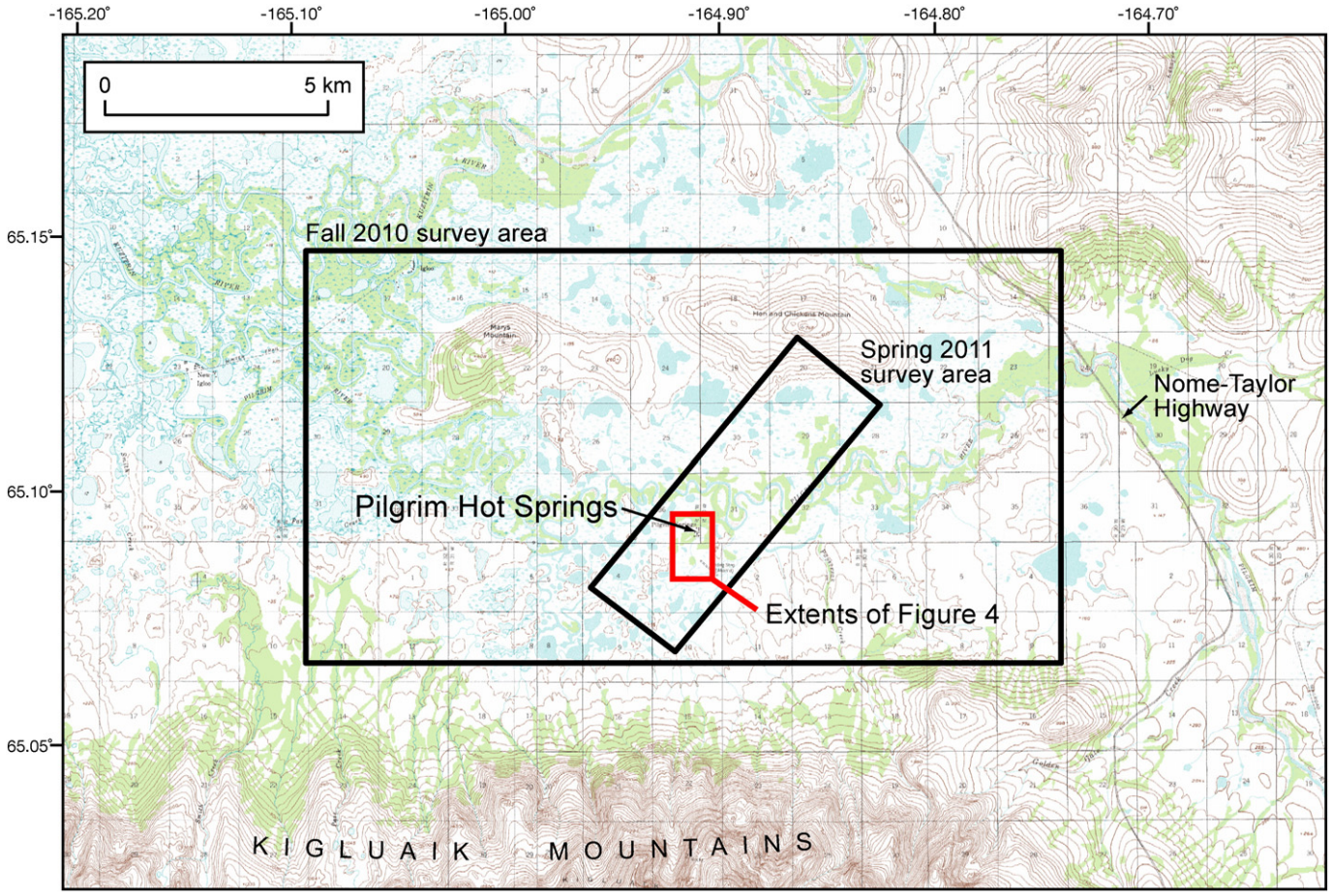

Fig. 3. Extents of FLIR survey areas at Pilgrim Hot Springs; the red lines indicate the extents of the airborne thermal and optical images presented in Fig. 4.

320m (Miller et al., 2013). The sedimentary infill comprises of interbedded fluvial sands and gravels eroded from the surrounding mountains, glaciofluvial deposits and lacustrine muds and silts (Miller et al., 2013; Woodward-Clyde Consultants, 1983). Lithologies exposed in the Kigluaik Mountains, and on Hen and Chicken and Mary's mountain include high grade meta-sedimentary and meta-igneous rocks (paragneiss and orthogneiss) of Paleozoic and Proterozoic age as well as granitic plutons that were emplaced during the Cretaceous (Till et al., 2010). The source and up-flow zone of the geothermal waters at Pilgrim Hot Springs have thus far not been identified. Normal faulting and nearby 2.5 Ma basaltic volcanism led Turner and Swanson (1981) to propose a rift model for this part of the Seward Peninsula that suggests basic intrusions could provide the heat source for the thermal waters (Liss & Motyka, 1994). Alternatively, the radiogenic decay of Cretaceous granitic plutons may be the heat source for the geothermal fluids as is inferred for other hot springs of the Central Alaskan Hot Springs Belt (Kolker, 2008).

3. Materials and methods

3.1. Measurement of hot spring heat fluxes and outflow rates using airborne TIR data

3.1.1. Data acquisition

Airborne TIR imagery (~1 m pixel size) was acquired over Pilgrim Hot Springs using a fixed-wing plane during two daytime airborne surveys in Fall 2010 (10th September) and early Spring 2011 (29th April) (Fig. 3). Two surveys were flown to assess seasonal variations in outflow of thermal waters and address the broader mission objectives of mapping surface geothermal phenomena outside of the known hot springs area. The Fall 2010 survey was flown at an altitude of ~1000 m above ground level (AGL) covering a ~180 km^2 for the purposes of providing observations for the larger study area. The Spring 2011 survey was flown at a lower altitude (~750 m AGL) to provide higher spatial resolution TIR imagery for a smaller ~16 km^2 survey area encompassing the immediate vicinity of the known geothermal area.

Broadband TIR images were acquired using a FLIR Systems A325 camera that was fixed through the belly port-hole of the plane. The camera records emitted TIR radiation in the 7.5–13 μm wavelength region using a 320 × 240, uncooled, microbolometer focal plane array (FPA). A 25° lens was used with the FLIR camera that resulted in a horizontal field of view (HFOV) of 443 m and pixel size of 1.39 m for the 1000 m AGL survey and HFOV of 332 m and pixel size of 1.04 m for the 750 m AGL survey. A laptop computer running the FLIR ThermaCAM Researcher Professional (Version 2.9) software was used to control the A325 during the flights. The camera was setup to record temperatures in the −20 to 120 °C calibration range that was appropriate for the environmental conditions and variety of hot spring temperatures that were expected during the two flights. TIR imagery was recorded at a frame rate of 5 Hz providing ~80% overlap in the along-track direction. Flight lines were planned to ensure 30% across-track overlap thus providing complete coverage of TIR imagery for the survey areas.

To provide context for the TIR imagery we also acquired optical imagery using a 12.1 megapixel Nikon D700 Digital SLR camera. The D700 was installed along with the A325 through the belly port-hole

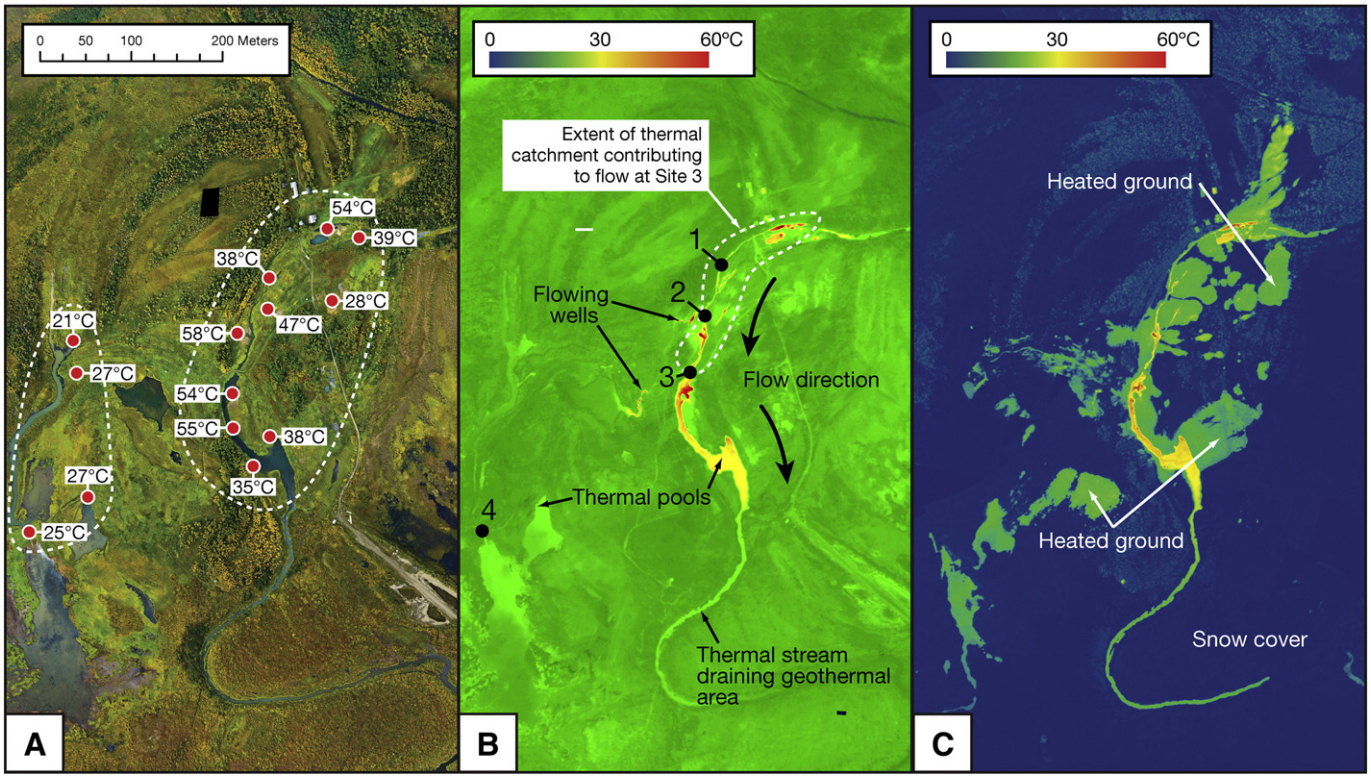

Fig. 4. Aerial imagery for the study area at Pilgrim Hot Springs; (A) optical data acquired with a Nikon D700 camera showing locations and temperature of hot springs mapped from the thermal imagery (red dots) that form two broad groups (dashed outlines); (B) thermal imagery acquired with a FLIR A325 camera on 09/10/2010; (C) thermal imagery acquired on 04/28/2011. The thermal data outlines the location of hot springs, seeps, thermal pools, and thermal streams draining the geothermal area. Heated ground is manifested as areas of anomalous snow melt in the winter-time thermal image (C). The sites of field hot spring flow measurements are shown as black dots on (B).

of the plane and the camera used a calibrated 85 mm lens with focus fixed at infinity yielding visible images with a HFOV and pixel resolution of 420 m and 15 cm, and 318 m and 10 cm for the 1000 and 750 m AGL surveys, respectively. A second laptop computer and Topoflight Navigator software (TopoFlight Systems, 2013) was used to trigger the Nikon D700 camera at pre-defined intervals on the flight path to achieve 30% along-track overlap. A GPS/INS system (Crossbow NAV-440) was used to continuously record positional and exterior orientation parameters during the surveys.

Prior to and during the airborne survey periods various in-situ data were acquired as input into processing, calibration, and analysis of the TIR imagery. To provide ground control points that would be recognizable within the TIR imagery we placed and recorded the GPS positions of a number of aluminum foil 'space-blankets'. These targets have low emissivity properties and were readily discernible in the TIR imagery due to their strong brightness temperature contrast with the surrounding natural land cover. As input into pre-processing and application of the heat budget model to the FLIR data, we recorded atmospheric temperature, humidity and wind speed using a portable weather meter (Kestrel 3000 Wind Meter). The temperatures of different surface features, such as snow and thermal pools, was also recorded using temperature loggers (HOBO) and hand-held temperature probes (Tegam) for the purposes of calibration and validation of FLIR-derived surface temperature values.

3.1.2. Pre-processing of TIR data

Initial pre-processing of the TIR imagery involved the conversion of at-sensor-radiance values to surface temperature using a first-order correction for atmospheric absorption, surface emissivity and ambient temperature effects using the ThermaCAM Researcher software. Inputs into this procedure included the distance to target (i.e. altitude AGL), ambient air temperature and relative humidity that were recorded at the time of flight overpass. An emissivity value of 0.98 was used for the first-order correction that is an appropriate value for water (Smikrud et al., 2008). The calibrated surface temperature data were exported from the ThermaCAM Researcher software using the FLIR Public File (FPF) format and time stamps for each frame were extracted using a procedure implemented in Interactive Data Language (IDL). The time interval necessary to achieve ~30% along-track overlap was calculated and then the frame with the smallest roll value in each interval was selected as queried from the GPS/INS log. The TIR image subset was then registered and mosaicked with EnsoMOSAIC UAV Pro software (MosaicMill, 2013) using the GPS coordinates and exterior orientation information for each frame retrieved from the GPS/INS log, estimated camera calibration parameters for the FLIR A325 camera, and the GPS positions of the 'space-blanket' ground control points. The registration and mosaicking of the D700 visible imagery was undertaken in the same manner but using precise camera interior orientation parameters derived from a prior camera calibration. The resultant TIR and visible image mosaics displayed some mis-registration (5–10 m) that probably reflects the lack of a stabilized camera mount and the fact that triggering of the cameras was not precisely synchronized. This was not considered a significant issue as the visible imagery was not used as a direct input to analysis of the TIR data.

Comparison of the atmospherically corrected FLIR surface temperature data with in-situ temperature measurements (of thermal pools, areas of snow, and exposed ground) taken at the time of the flight overpass showed that the airborne data consistently underestimated the surface temperature values by ~2–3 °C (Prakash et al., 2010). These differences were corrected by performing a linear regression of in-situ measured temperature values against FLIR-measured temperature values for a series of ground targets.

For the known geothermal area, the mosaicked FLIR data from the two surveys enables clear delineation of hot springs, thermal pools,

and thermal streams (Fig. 4). Numerous hot springs are mapped from the thermal data that form two broad groupings: 1) a zone of N–S aligned springs that have the hottest water surface temperatures (35–58 °C) and outflow into a single elongated thermal pool at the site; 2) a second roughly N–S aligned swath of several cooler springs (21–27 °C) that are located further to the west. The mosaicked TIR imagery indicates that the surface hydrology of the springs and hot pools at Pilgrim Hot Springs is appropriate for the use of a thermal budget modeling approach; the water in the hot pools that is fed from the hot springs cools to ambient temperatures with distance from these sources and does not appear to mix with other meteoric waters by the time it has cooled. Consequently, there is limited heat transfer by advection and thermal waters are assumed to cool mainly by radiation, evaporation and sensible heat transfer.

3.1.3. Application of thermal budget model to TIR data

A simplified, steady-state thermal budget model was used to calculate the hot spring heat flux sustaining the temperature of the thermal waters above ambient conditions. This analysis was restricted to the known geothermal area as no other obvious thermally anomalous waters were observed outside of this area. The calculation of the hot spring heat flux involved first delineating pixels corresponding to the thermal waters (Fig. 4); a simple threshold of high temperature values (16 and 8.5 °C for the Fall 2010, and Spring 2011 TIR data, respectively) followed by limited manual editing (using the optical image mosaic as reference) was used to create masks that were applied to remove all pixels not corresponding to thermal waters in the calibrated FLIR imagery. In particular, areas of thermal water representing outflow from drilled geothermal wells (Fig. 4) were masked as the aim of the research was to assess the heat flux and flow rate from the naturally occurring hot springs. The temperature threshold values were selected by estimating the mean temperature value of surface pools at ambient conditions. In the case of the Fall 2010 data, we calculated the average temperature of nearby surface ponds and lakes. For the Spring 2011 data, this was not possible as non-geothermal waters were ice-covered so we used the temperature of the thermal water (in the main thermal stream draining the geothermal area) at the location where this appeared to cool to ambient temperatures from the Fall 2010 data: this area of water was ice-free in the Spring 2011 data.

For the data from the two surveys th(q_{sun})e hot spring heat flux density (q_{geo}), in units of W/m^2, was calculated on a per-pixel basis using the surface temperature of the thermal water as input into a simplified version of the heat budget formula (Eq. (1)). In calculating q_{geo}, the seepage (q_{seep}) term was ignored as it was considered to be negligible in relation to the geothermal/hot spring heat flux that was an assumption also made by Oppenheimer (1996) and Patrick et al (2004). We also assume that the heat flux associated with precipitation (q_{ppt}), incoming shortwave solar, and atmospheric longwave radiation (q_{sky}) can be estimated from the average temperature of non-geothermal surface ponds or lakes. In the absence of heat input from the hot springs the temperature of these bodies of water will mainly be related to precipitation, solar and atmospheric fluxes. Based upon this assumption q_{geo} is calculated as the difference between the total heat loss for the thermal water at the temperature of the pixel and the heat loss for an equivalent area of non-geothermal waters at an average 'ambient' surface temperature. This modification removes the need to explicitly calculate incoming solar (q_{sun}), and atmospheric (q_{sky}) fluxes that would require the use of physical models (e.g. MODTRAN) and the results of which would be highly sensitive to the atmospheric model parameters (Patrick et al., 2004). Using these assumptions q_{geo} is calculated using:

$$q_{geo} = \left(q_{rad} + q_{evap} + q_{sens}\right) - \left(q_{radAmb} + q_{evapAmb} + q_{sensAmb}\right) \quad (2)$$

where q_{rad}, q_{evap}, and q_{sens} are radiative, evaporative and sensible heat flux densities for the thermal water pixel, and q_{radAmb}, $q_{evapAmb}$, and $q_{sensAmb}$ are radiative, evaporative, and sensible heat flux densities calculated at the mean temperature of ambient surface waters. For the Fall 2010 and Spring 2011 surveys, temperature values of 16 and 8.5 °C were respectively used as the average values for waters at ambient surface conditions that represent the same values used previously to delineate thermal from ambient waters.

Both the wind (forced convection) and air–water temperature difference (free convection) are the driving forces behind evaporative and sensible heat losses from the surface of a body of heated water. The formula of Ryan et al. (1974) was used to calculate these heat losses under both free and forced convective conditions at the temperature of the thermal water pixel:

$$q_{evap} + q_{sens} = \left[\lambda(T_{sv} - T_{av})^{1/3} + b_0 W_2\right] \cdot [e_s - e_2 + C(T_s - T_a)] \quad (3)$$

where $\lambda = 2.7$ (a constant in units of W m^{-2} mbar^{-1} [°C]$^{-1/3}$), $b_0 = 3.2$ (a constant in units of W m^{-2} mbar^{-1} [m/s]$^{-1}$), W_2 = wind speed at 2 m height (m s^{-1}), e_s = vapor pressure of water at T_s (mbar), e_2 = vapor pressure of water at 2 m height (mbar), $C = 0.61$ (a constant in units of mbar [°C]$^{-1}$), T_s = water surface temperature (°C), T_a = air temperature (°C), T_{sv} = virtual water surface temperature (°C), and T_{av} = virtual air temperature (°C). The same formula was used to calculate the evaporative and sensible heat losses at the mean ambient surface water temperature ($q_{evapAmb} + q_{sensAmb}$) by substituting T_s and T_{sv} with the corresponding ambient temperature values in the equation. Inputs into both sets of equations include measurements of wind speed and air temperature that were recorded during the period of flight overpass for the two surveys.

Radiative heat loss (q_{rad}) was calculated at the temperature of the thermal water pixel using the Stefan–Boltzmann equation:

$$q_{rad} = \varepsilon \sigma T_s^4 \quad (4)$$

where ε is emissivity (0.98, that is appropriate for water), σ is the Stefan–Boltzmann constant (5.670373×10^{-8} W/m^2/K^4), and T_s is the water surface kinetic temperature. Using the same formula the radiative heat loss was calculated at the mean ambient surface temperature (q_{radAmb}) by substituting T_s with the ambient water temperature value.

For the Fall 2010 and Spring 2011 surveys, the total hot spring heat flux (Φ_{geo}) was calculated by multiplying the per-pixel hot spring heat flux densities (q_{geo}) by the corresponding pixel area and summing all the heat flux values for the thermal water pixels. The values of Φ_{geo} (converted to KW units) for the two surveys were used to estimate the corresponding mass flow rate ($\dot{m}$ in units of kg/s) of the hot springs assuming a fixed temperature value for the geothermal waters with the following equation:

$$\dot{m} = \Phi_{geo}/(h_s - h_{amb}) \quad (5)$$

where h_s and h_{amb} are the enthalpy of water (in kJ/kg) at the hot spring (81.3 °C) and ambient water temperature respectively. These mass flow rates were converted to a volumetric outflow rate in units of liters/minute using the density of water at the hot spring temperature to facilitate comparison of the FLIR outflow rates with in-situ measurements.

3.2. Field measurements of hot spring heat fluxes and outflow rates

The validation of hot spring heat fluxes and outflow rates derived from the FLIR data was undertaken using a variety of field measurements. It is not feasible to directly measure the outflow rate of the hot springs; instead, this is derived from estimates of the volumetric flow rates and water temperatures within thermal streams draining

the geothermal area (Fig. 4). Harrison and Hawkins (1980) estimated the hot spring outflow rate and heat flux using volumetric flow measurements at Site 1 (Fig. 4) acquired with a current meter. They assumed that the flow in this thermal stream comprised of both thermal and surface meteoric waters and used the measured temperature in the thermal stream to determine the hot spring outflow rate from the conservation of water and heat. The hot spring heat flux was determined as the product of water heat capacity, flow rate and the temperature difference between water at 0 °C and the hot spring temperature (81.3 °C) (Harrison & Hawkins, 1980). Measurements of the flow rate in thermal streams (at Sites 1, 2, and 4; Fig. 4) were undertaken in the early 1980s using a series of V-notch shaped weirs that provided estimates of the hot spring heat flux of ~2 MW of thermal energy (Woodward-Clyde Consultants, 1983).

For the current research, estimates of the hot spring outflow rate were recorded during field investigations in Summer 2011 and 2012 using flow rate measurements through a culvert at Site 3 that is located on the main N–S aligned thermal stream draining the geothermal area (Fig. 4). Measurement of the hot stream flow rate involved recording the cross-sectional area of the water in the culvert and the velocity using a current meter. Our estimates of the hot spring outflow rate assume that all waters flowing through the culvert at Site 3 originate from the hot springs in the upstream thermal catchments with negligible contributions of meteoric water. Field observations and the spatial distribution of thermal waters mapped from the FLIR imagery (Fig. 4) indicate that mixing of hot spring waters with other surface cold streams does not occur in the geothermal area that contradicts the observations of Harrison and Hawkins (1980). Hence, it is assumed that the flow rate measured through the culvert at Site 3 represents the total outflow from the hot springs in the upstream thermal catchment (Fig. 4). This was used to estimate the hot spring heat flux (Table 2) assuming an ambient water temperature of 15 °C (derived from field measurements of surface pools) with:

$$\Phi_{geo} = \dot{m}(h_s - h_{amb}) \quad (6)$$

The field-derived hot spring outflow rates and associated heat fluxes show considerable variability particularly between the 1979–1982 and 2011–2012 measurement sets that may be explained by: 1) the differing locations and techniques used to record the thermal stream flow rates; 2) seasonal differences in the hot spring outflow rates possibly related to varying hydrological conditions; 3) potential longer-term variation in the surface expressions or output of the geothermal system. Given these factors, validation of the FLIR results has focused on the 2011–2012 field data, although the 1979–1982 results provide important context and reference data. The 2011 and 2012 field-derived hot spring outflow rates/heat fluxes generally show good agreement with variation that may be explained by seasonal hydrological factors.

4. Results and discussion

4.1. Comparison of FLIR- and field-derived hot spring heat fluxes and outflow rates

A summary of the results of hot spring heat flux and outflow rate calculations derived from the fall and spring FLIR data is presented in Table 1. The results of existing and recent field measurements of the outflow rate of the hot springs and associated hot spring heat flux estimates are presented in Table 2. The results from the two FLIR surveys (Table 1) show good agreement with slightly higher estimates of heat flux for the Spring 2011 survey data. Although the FLIR-derived estimates are higher than the values measured in the field during 2011–2012 this is expected given the differences in what is actually being measured by the two approaches. The 2011–2012 field data records the outflow from a subset of the hot springs in the upstream thermal catchment of the culvert at Site 3 (Fig. 4). In contrast, the synoptic coverage of the FLIR imagery maps all areas of thermal water so the hot spring heat flux and outflow rates are representative for all the hot springs in the geothermal area.

To provide a more representative comparison of the FLIR and field results two additional analyses were undertaken. Firstly, the hot spring heat flux/outflow rate calculations were restricted to just the main thermal pool that is drained by the thermal stream, which flows through the culvert at Site 3; other areas of thermal water (e.g. the thermal pools located further to the west) were excluded from the analysis using a simple mask applied to the FLIR data. The analysis was undertaken for the whole thermal pool/stream that included the thermal waters upstream and downstream of the culvert at Site 3. The results (Table 1) show better agreement between the field- and FLIR-derived estimates of hot spring heat flux/outflow rate. However, there are several hot springs downstream of Site 3 (Fig. 4) that would have contributed to the FLIR estimate but would not have been included in the field measurements. It would be expected that the FLIR estimate would be higher given the additional contribution from these thermal waters, which is not the case.

Secondly, the hot spring heat flux for the thermal catchment upstream of Site 3 (Fig. 4) was calculated from the FLIR data (Table 1) and the average advective heat flux (from the 2010 and 2011 field data) through the culvert at Site 3 was estimated using Eq. (6) and the average field temperature of the thermal stream flowing through the culvert (34 °C). The sum of the heat fluxes (i.e. advective + radiative, evaporative, and sensible calculated from the FLIR) provides an estimate of the total hot spring heat flux for the thermal catchment upstream of site 3 that was compared against the value estimated directly from the flow rate (i.e. at the hot spring temperature of 81.3 °C at this site; Table 2). The results for the Fall 2010 and Spring 2011 FLIR surveys indicate total heat losses of 1.79 MW and 1.71 MW respectively for the thermal catchment upstream of Site 3 that is lower than the average hot spring heat flux (~3.2–3.7 MW) estimated directly from the flow measurement at this locality. The explanations for these discrepancies include: 1) the FLIR method is underestimating the hot spring heat flux; 2) the flow rate measurements at Site 3 overestimate the hot spring

Table 1
Summary of input parameters and results of hot spring heat flux and outflow rates calculated from airborne FLIR imagery for Pilgrim Hot Springs.

FLIR survey date	Hot springs analyzed	Hot water area (km^2)	Ambient T_s (°C)	T_a (°C)	W_2 ($m\ s^{-1}$)	Φ_{geo} (MW)	Outflow rate at 81.3 °C (l/min)
09/10/2010	All	0.033	15.0	16	0.58	4.65	1015.06
	Main thermal stream	0.015	15.0	16	0.58	3.25	708.95
	Catchment upstream of Site 3	0.003	15.0	16	0.58	0.86	187.50
04/28/2011	All	0.029	8.5	7	0.50	4.68	937.44
	Main thermal stream	0.014	8.5	7	0.50	3.66	732.04
	Catchment upstream of Site 3	0.002	8.5	7	0.50	0.75	149.51

Table 2
Summary of field-measured hot spring outflow rates and heat flux estimates; the sites of field measurements are indicated on Fig. 4.

Measurement date	Site	Φ_{geo} (MW)	Outflow rate (l/min)	Comments	Reference
06/19/1979	1	1.40	264.00	Determined from mixing of hot and cold waters	Harrison and Hawkins (1980)
07/05/1982	1	–	67.96		Woodward-Clyde Consultants (1983)
07/05/1982	2	–	190.29		Woodward-Clyde Consultants (1983)
07/05/1982	4	–	815.52		Woodward-Clyde Consultants (1983)
07/05/1982		2.00	–	Estimated total heat flux of hot springs	Woodward-Clyde Consultants (1983)
08/30/2011	3	3.05	662.40		This paper
07/05/2012	3	3.67	798.60		This paper

outflow rate due to contributions from surface meteoric waters; 3) there is variation in the hot spring outflow rate between the FLIR surveys and the period when the field measurements were recorded.

4.2. Sources of error in FLIR-derived hot spring heat fluxes and outflow rates

To address the potential that the FLIR method is underestimating the hot spring heat fluxes and outflow rates and investigate the sensitivity of the thermal budget model to input parameters, the models were re-run while systematically varying values of the wind speed (W_2) and ambient water temperature (T_s). Heat fluxes associated with free convection are linearly related to the temperature difference between the water surface (T_s) and air (T_a). In the model, the hot spring heat flux per pixel is calculated as the difference between the sum of the heat fluxes for thermal water and the sum of the heat fluxes for water at ambient surface temperatures. Assuming fixed temperature values for thermal and ambient water then variations in the air temperature (T_a) will not affect the net free convective heat flux as T_s–T_a are the same. For this reason, it was not necessary to address variation in T_a within the model runs.

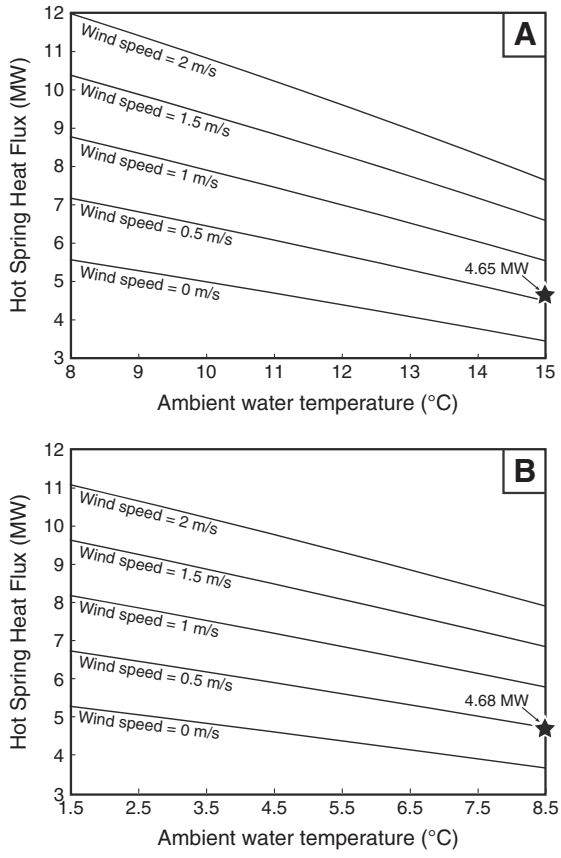

Fig. 5. Variation in total hot spring heat flux (MW) calculated from airborne FLIR data acquired on 09/10/2010 (A), and 04/28/2011 (B) as a function of the ambient water temperature (T_s) and wind speed (W_2) using fixed values for ambient air temperature (T_a) of 16 °C (A) and 7 °C (B); the black star indicates the parameters used to calculate the total hot spring heat flux in Table 1 that includes wind speed measurements recorded at the time of flight overpass.

The results (Fig. 5) demonstrate that wind speed is the dominant control on the hot spring heat fluxes and variation in the ambient water temperature is less significant. Assuming fixed ambient water temperatures (15 and 8.5 °C for the fall and spring FLIR data respectively) then modest increases in wind speed from the field-derived value of ~0.5 m/s to 1 m/s and 2 m/s would result in average hot spring heat flux increases of 20% and 66% respectively. As wind speeds were recorded at the instant of the flight overpasses there is potential that these may not be representative of the longer-term average conditions, which may be more relevant to the thermodynamics of the thermal pools/streams; i.e. an average wind speed over the course of a day or week that includes gusting conditions may provide a more representative parameterization, which is a shortcoming of our method. When compared to annual average wind speed values for comparable in-land areas of Alaska that range from 2 to 3 m/s (National Climatic Data Center, 2008), the values of ~0.5 m/s used in the heat budget models appear to be low that would result in underestimates of the hot spring heat flux using the FLIR method. Although there is potential that errors in the ambient water temperature values could also affect the results, this is considered to be less significant than errors in the wind speed. For the Fall 2010 FLIR data, the ambient water temperature could be accurately determined from the surface non-thermal pools and any overestimation in the model value (i.e. on the order of several degrees) would lead to only a modest increase in the hot spring heat flux calculated from the FLIR data (Fig. 5). There is more potential for overestimation of the ambient water temperature value used within the heat budget model applied to the Spring 2011 FLIR data as this parameter was difficult to determine given the ice-covered wintertime conditions. The value used in the model was determined from the water temperature at the location on the thermal pools/streams just before the waters became ice-covered. As such, this is likely to be an overestimated value that implies the FLIR-derived heat fluxes and outflow rates from the Spring 2011 data are underestimates. This said, even assuming larger error in the ambient water temperature value the effects of errors in wind speed still has a much larger impact on the heat flux and outflow rates estimated from the FLIR data.

The values of wind speed and ambient water temperature were also systematically varied in calculating the hot spring heat flux for just the thermal catchment upstream of Site 3 (Fig. 4): for this case the fixed value of average advective heat flux (i.e. for waters at 34 °C) previously determined from flow measurements through the culvert at Site 3 was added to the model-dependent FLIR-derived values of hot spring heat flux. The results (Fig. 6) also demonstrate that wind speed is the dominant control on the hot spring heat flux estimates for this thermal catchment although the wind speed value would have to be considerably higher to match the values estimated from the field measurements (i.e. calculated at the hot spring temperature of 81.3 °C; Table 2). Assuming a fixed ambient water temperature (15 and 8.5 °C for the fall and spring data respectively), then

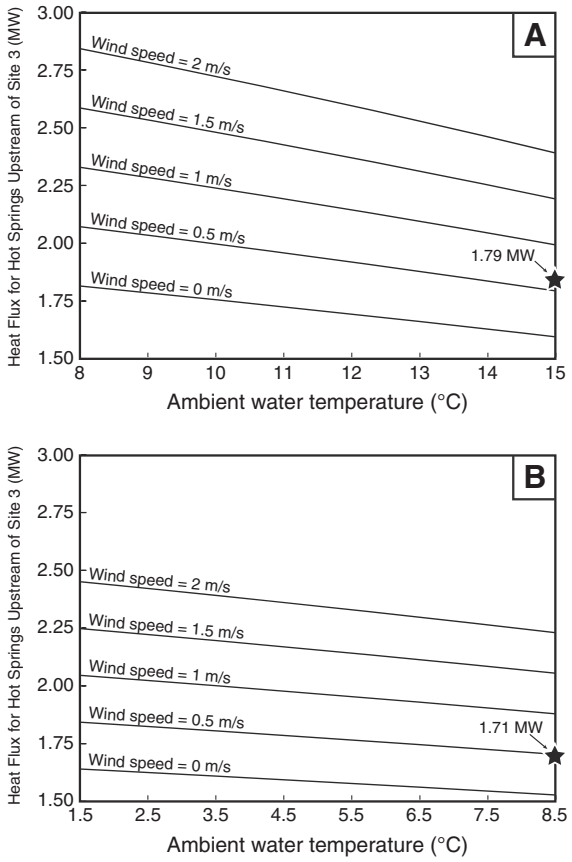

Fig. 6. Variation in the hot spring heat flux (MW) for the catchment upstream of Site 3 (MW) calculated from airborne FLIR data acquired on 09/10/2010 (A), and 04/28/2011 (B) and direct measurements of advective heat loss through the culvert at site 3 as a function of the ambient water temperature (T_s) and wind speed (W_2) using fixed values for ambient air temperature (T_a) of 16 °C (A) and 7 °C (B); the black star indicates the parameters used to calculate the total hot spring heat flux in Table 1 that includes wind speed measurements recorded at the time of flight overpass.

the wind speed values would have to rise to ~5 m/s and ~4.25 m/s for the fall and spring FLIR data respectively to produce the same hot spring heat flux as estimated from the field measurements for the thermal catchment upstream of Site 3. Assuming that this much higher value for wind speed is correct, then the heat flux for all the hot springs as estimated from the FLIR data would increase to 13.93 MW and 12.60 MW for the fall and spring data respectively. These values are ~180% higher than those estimated using the wind speeds measured at the time of flight overpass (Table 1). It is considered that such high values are unlikely and may be related to overestimation of the hot spring heat flux/outflow rate from the 2011/2012 in-situ measurements perhaps due to contributions to the water flow from precipitation and surface run-off or to incorrect assumptions about the temperature of the hot springs in calculating the hot spring heat flux. The absence of concurrent in-situ flow rate measurements and FLIR observations is one limitation of the current work and something that future studies should seek to address.

5. Conclusions

Although direct comparisons of the 2011/2012 field- and 2010/2011 FLIR-derived estimates of hot spring heat fluxes and outflow rates are subject to a number of uncertainties, including the varying dates of data acquisition and fundamental differences in what is actually being measured, these do suggest the FLIR approach underestimates the hot spring heat flux when the heat budget model is parameterized with the wind speeds recorded at the time of the flight overpass. The total average hot spring heat flux (of the two surveys) of ~4.7 MW and discharge rate of ~976 l/min derived from the FLIR data (Table 1) using the in-situ wind speed values are therefore likely to be conservative estimates. Assuming higher wind speeds (1.5 m/s) that may be more representative of longer-term, in-land Alaskan conditions then there is closer agreement between the field- and FLIR-derived estimates. Using this wind speed value the hot spring heat flux and outflow rates calculated from the FLIR data are estimated at ~6.7 MW and ~1400 l/min, respectively. These values are higher than estimates derived directly from field measurements as synoptic coverage of the FLIR imagery maps all thermal waters; in contrast, the field estimates correspond only to subsets of the hot springs and specific thermal catchments within the geothermal area. Comparison of the field- and FLIR-derived results for a specific hot stream catchment are broadly consistent but do show differences that may be explained by errors in the field-derived estimates of hot spring heat flux, variation in the output between the dates when the FLIR and field measurements were recorded, or due to errors in the FLIR estimates most likely related to underestimation of wind speeds.

This study has demonstrated the potential of using airborne TIR imagery acquired with a broadband FLIR camera to quantify the heat flux and outflow rate of hot springs using a case study of the Pilgrim Hot Springs geothermal system in western Alaska. This approach is based upon the use of a simplified, steady-state, heat budget model that accounts for radiative, evaporative, and sensible heat losses from areas of thermal water to derive the heat flux maintaining the temperature of these waters above ambient conditions. Given the issues associated with estimating the hot spring heat flux from field measurements, we consider that our FLIR-based approach provides a more reliable, simpler, and more direct approach to estimating the hot spring heat flux. Beyond the obvious benefit of the synoptic coverage of remotely sensed TIR imagery, this approach can be employed where direct measurements of hot spring outflow rates would be difficult to acquire such as when thermal waters are not confined to well-defined channels or the outflow rates are low. In addition, using the temperature and spatial distribution of thermal waters is a conceptually more robust and direct way to estimate the hot spring heat flux than measurements of a secondary parameter such as the flow rate in thermal streams draining geothermal areas that may be affected by meteoric water inputs. As a result of this work, we have provided new estimates of the hot spring heat flux and outflow rate that will support improved reservoir modeling and resource assessment of the Pilgrim Hot Springs geothermal system. This approach has significant potential as a rapid and repeatable method for quantitative investigations of spring-dominated geothermal systems supporting resource assessment, and long-term monitoring.

Acknowledgments

The research was funded by the Department of Energy Geothermal Technologies Programme (CID: DE-EE0002846) and the Alaska Energy Authority Renewable Energy Fund Round III. We are grateful to Jessie Cherry and Matt Nolan for their efforts on airborne system integration as well as data acquisition and would also like to thank Markus Mager, Forrest Kirst, Peter Illig, Kate Schaefer and Jonathan O'Toole for their work during the airborne surveys.

References

Alaska Center for Energy and Power (2012). *Validation of innovative exploration techniques, Pilgrim Hot Springs, Alaska — Phase 1 final report (DE-EE0002846).*

Allis, R. G., Nash, G. D., & Johnson, S. D. (1999). Conversion of thermal infrared surveys to heat flow: Comparisons from Dixie Valley, Nevada, and Wairakei, New Zealand. *GRC Transactions, 23.*

Bromley, C. J., van Manen, S. M., & Mannington, W. (2011). Heat flux from steaming ground: Reducing uncertainties. *Thirty-Sixth Workshop on Geothermal Reservoir Engineering.* Stanford, California: Stanford University.

Ellis, A. J., & Wilson, S. H. (1955). The heat from the Wairakei–Taupo thermal region calculated from the chloride output. *New Zealand Journal of Science and Technology*, *B36*, 622–631.

Harrison, W., & Hawkins, D. (1980). Water and heat flow measurements and their relationship to power estimates at Pilgrim Springs, Alaska. In D. L. Turner, & R. B. Forbes (Eds.), *A geological and geophysical study of the geothermal energy potential of Pilgrim Springs, Alaska. Geophysical Institute Report UAG R-271*.

Heasler, H., Jaworowski, C., & Foley, D. (2009). Geothermal systems and monitoring hydrothermal features. In R. Young, & L. Norby (Eds.), *Geological monitoring*. Boulder, Colorado: Geological Society of America.

Hernández, P., Pérez, N., Varekamp, J., Henriquez, B., Hernández, A., Barrancos, J., et al. (2007). Crater lake temperature changes of the 2005 eruption of Santa Ana Volcano, El Salvador, Central America. *Pure and Applied Geophysics*, *164*(12), 2507–2522.

Hodder, D. T. (1970). Application of remote sensing to geothermal prospecting. *Geothermics*, *2*(1), 368–380.

Ingebritsen, S. E., Galloway, D. L., Colvard, E. M., Sorey, M. L., & Mariner, R. H. (2001). Time-variation of hydrothermal discharge at selected sites in the western United States: Implications for monitoring. *Journal of Volcanology and Geothermal Research*, *111*(1–4), 1–23.

Kolker, A. (2008). *Geologic setting of the Central Alaskan Hot Springs Belt: Implications for geothermal resource capacity and sustainable energy production.* Fairbanks, Alaska: University of Alaska Fairbanks (PhD).

Liss, S. A., & Motyka, R. J. (1994). Pilgrim Springs KGRA, Seward Peninsula, Alaska: Assessment of fluid geochemistry. *Geothermal Resources Council Transactions*, *18*.

Miller, J. K., Prakash, A., Daanen, R., Haselwimmer, C. E., Whalen, M., Mager, M., et al. (2013). Geologic model of the geothermal anomaly at Pilgrim Hot Springs, Seward Peninsula, Alaska. *Stanford Geothermal Workshop 2013, Stanford, California*.

Mongillo, M. (1994). Aerial thermal infrared mapping of the Waimangu–Waiotapu geothermal region, New Zealand. *Geothermics*, *23*(5/6), 511–526.

MosaicMill (2013). MosaicMill — EnsoMOSAIC. Retrieved 1/24/2013, from http://www.ensomosaic.com/

National Climatic Data Center (2008). Wind — Average wind speed (MPH). Retrieved 11/29, 2012, from http://www.ncdc.noaa.gov/oa/climate/online/ccd/avgwind.html

Obha, T., Hirabayashi, J., & Nogami, K. (1994). Water, heat and chloride budgets of the crater lake, Yugama at Kusatsu–Shirane volcano. *Japan Geochemical Journal*, *28*, 217–231.

Oppenheimer, C. (1996). Crater lake heat losses estimated by remote sensing. *Geophysical Research Letters*, *23*(14), 1793–1796.

Oppenheimer, C. (1997a). Remote sensing of the colour and temperature of volcanic lakes. *International Journal of Remote Sensing*, *18*(1), 5–37.

Oppenheimer, C. (1997b). Ramifications of the skin effect for crater lake heat budget analysis. *Journal of Volcanology and Geothermal Research*, *75*(1–2), 159–165.

Patrick, M., Dean, K., & Dehn, J. (2004). Active mud volcanism observed with Landsat 7 ETM+. *Journal of Volcanology and Geothermal Research*, *131*(3–4), 307–320.

Prakash, A., Nolan, M., Schaefer, K., Haselwimmer, C. E., & Holdmann, G. (2010). Geothermal exploration in Pilgrim, Alaska: First results from remote sensing studies. Abstract no: V13B-2350. *AGU Fall Meeting*. San Francisco: American Geophysical Union.

Richards, M., & Blackwell, D. D. (2002). The Nevada story: Turning loss into gain. *Geothermal Resources Council Bulletin*, *31*(3), 107–110.

Ryan, P. J., Harleman, D. R. F., & Stolzenbach, K. D. (1974). Surface heat loss from cooling ponds. *Water Resources Research*, *10*(5), 930–938.

Seielstad, C., & Queen, L. (2009). Thermal remote monitoring of the Norris Geyser Basin, Yellowstone National Park. *Final Report for the National Park Service Cooperative Ecosystem Studies Unit, Agreement No. H1200040001* (38 pp.).

Smikrud, K., Prakash, A., & Nichols, J. (2008). Decision based fusion for improved fluvial landscape classification using digital aerial photographs and forward looking infrared images. *Photogrammetric Engineering and Remote Sensing*, *74*(7), 903–911.

Till, A. B., Dumoulin, J. A., Werdon, M. B. & Bleick, H. A. (2010). Preliminary geologic map of the Seward Peninsula, Alaska, and accompanying conodont data. Sheet 1, scale 1:500,000, US Geological Survey, Anchorage, AK.

TopoFlight Systems (2013). TopoFlight 3D planning software. Retrieved 1/24/2013, from http://www.topoflight.com/

Turner, D. L., & Forbes, R. B. (1980). A geological and geophysical study of the geothermal energy potential of Pilgrim Springs, Alaska. *University of Alaska, Geophysical Institute Report UAG R-271*.

Turner, D. L., & Swanson, S. (1981). Continental rifting — A new tectonic model for the central Seward Peninsula. In E. Wescott, & D. L. Turner (Eds.), *Geothermal reconnaissance survey of the central Seward Peninsula, Alaska*. Fairbanks, Alaska: Geophysical Institute, University of Alaska.

Vaughan, R. G., Keszthelyi, L. P., Lowenstern, J. B., Jaworowski, C., & Heasler, H. (2012). Use of ASTER and MODIS thermal infrared data to quantify heat flow and hydrothermal change at Yellowstone National Park. *Journal of Volcanology and Geothermal Research*, *233–234*, 72–89.

Wescott, E., & Turner, D. C. (1981). Geothermal reconnaissance survey of the central Seward Peninsula, Alaska. *University of Alaska, Geophysical Institute Report UAG R-284*.

Wisian, K. W., Blackwell, D. D., & Richards, M. (2001). Correlation of surface heat loss and total energy production for geothermal systems. *Geothermal Resources Council Transactions*, *25*.

Woodward-Clyde Consultants (1983). *Geothermal energy development at Pilgrim Springs, Alaska. Phase II: Results of drilling, testing and resource confirmation.*